

PUBLISHED VERSION

Resistive wall tearing mode generated finite net electromagnetic torque in a static plasma

G. Z. Hao, Y. Q. Liu, A. K. Wang, M. Xu, H. P. Qu, X. D. Peng, Z. H. Wang, J. Q. Xu, and X. M. Qiu

© 2013 UNITED KINGDOM ATOMIC ENERGY AUTHORITY.

This article may be downloaded for personal use only. Any other use requires prior permission of the author and the American Institute of Physics. The following article appeared in *Physics of Plasmas* **21**, 012503 (2014) and may be found at doi: 10.1063/1.4861376



Resistive wall tearing mode generated finite net electromagnetic torque in a static plasma

G. Z. Hao, Y. Q. Liu, A. K. Wang, M. Xu, H. P. Qu, X. D. Peng, Z. H. Wang, J. Q. Xu, and X. M. Qiu

Citation: [Physics of Plasmas \(1994-present\)](#) **21**, 012503 (2014); doi: 10.1063/1.4861376

View online: <http://dx.doi.org/10.1063/1.4861376>

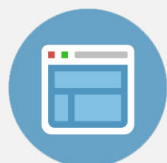
View Table of Contents: <http://scitation.aip.org/content/aip/journal/pop/21/1?ver=pdfcov>

Published by the [AIP Publishing](#)



Re-register for Table of Content Alerts

Create a profile.



Sign up today!



Resistive wall tearing mode generated finite net electromagnetic torque in a static plasma

G. Z. Hao,^{1,a)} Y. Q. Liu,² A. K. Wang,¹ M. Xu,¹ H. P. Qu,¹ X. D. Peng,¹ Z. H. Wang,¹ J. Q. Xu,¹ and X. M. Qiu¹

¹Southwestern Institute of Physics, Post Office Box 432, Chengdu 610041, China

²Euratom/CCFE Fusion Association, Culham Science Centre, Abingdon OX14 3DB, United Kingdom

(Received 11 September 2013; accepted 19 December 2013; published online 8 January 2014)

The MARS-F code [Y. Q. Liu *et al.*, Phys. Plasmas **7**, 3681 (2000)] is applied to numerically investigate the effect of the plasma pressure on the tearing mode stability as well as the tearing mode-induced electromagnetic torque, in the presence of a resistive wall. The tearing mode with a complex eigenvalue, resulted from the favorable averaged curvature effect [A. H. Glasser *et al.*, Phys. Fluids **18**, 875 (1975)], leads to a re-distribution of the electromagnetic torque with multiple peaking in the immediate vicinity of the resistive layer. The multiple peaking is often caused by the sound wave resonances. In the presence of a resistive wall surrounding the plasma, a rotating tearing mode can generate a finite net electromagnetic torque acting on the static plasma column. Meanwhile, an equal but opposite torque is generated in the resistive wall, thus conserving the total momentum of the whole plasma-wall system. The direction of the net torque on the plasma is always opposite to the real frequency of the mode, agreeing with the analytic result by Pustovitov [Nucl. Fusion **47**, 1583 (2007)]. When the wall time is close to the oscillating time of the tearing mode, the finite net torque reaches its maximum. Without wall or with an ideal wall, no net torque on the static plasma is generated by the tearing mode. However, re-distribution of the torque density in the resistive layer still occurs. © 2014 AIP Publishing LLC.

[<http://dx.doi.org/10.1063/1.4861376>]

I. INTRODUCTION

The tearing mode is one of the most important magneto-hydrodynamics (MHD) instabilities in magnetic confined plasmas. The tearing mode can lead to the deterioration of the confinement, mode locking to the external resistive wall, and plasma disruption.^{1–3} The onset of the neoclassical tearing mode (NTM) provides a limitation for achievable β (the ratio of the averaged plasma pressure to the magnetic pressure). It is known that the favorable averaged curvature of the equilibrium magnetic field has strong stabilization effect on the tearing mode. The tearing mode is unstable only when the tearing mode parameter Δ'_{ext} exceeds a critical positive value, in the presence of the favorable magnetic curvature and the finite pressure gradient.^{4–6}

This work numerically investigates the finite equilibrium pressure gradient effect (i.e., the GGJ-effect)⁴ on the resistive wall tearing mode, as well as the associated net electromagnetic (EM) torque produced by a rotating tearing mode that acts back on the (static) plasma. In this work, we solve the resistive MHD equations in a full toroidal geometry with no ordering assumptions, using the MARS-F code. It is confirmed that the plasma pressure has a stabilization effect on the tearing mode in the lower β_N region, which results from the favorable average curvature of the equilibrium magnetic field. The curvature affects the growth rate of the classical tearing mode through the modification of the inner layer solution.⁴ In addition, it is found that when β

approaches the no-wall beta-limit, the plasma pressure destabilizes the mode and helps to couple the tearing mode to global kink structures. The high plasma pressure (but lower than the no-wall β_N limit) induced coupled tearing-kink structure may be experimentally investigated, through the measurement of the island structure using, e.g., the electron cyclotron emission (ECE) diagnostic.

The physics of the EM torque on a rotating plasma has been investigated in details, e.g., in Refs. 7–12, where the torque appears as a momentum sink term. Reference 13 experimentally shows that a considerable amount of torque can be generated by the resistive activity in a tokamak plasma, based on the momentum exchange between the plasma and the resistive wall. In this work, the rotation of the tearing mode in a static plasma is induced by the strong curvature effect, which further generates a net torque. We note that certain physics aspects of the EM torque presented here, such as the dependence of the torque on the mode's frequency as well as on the wall penetration time, are similar to that predicted by earlier theories in Refs. 8, 11, and 14. The EM torque presented in this work may serve as a momentum source term, in addition to other possible sources, for generating intrinsic rotation in a tokamak plasma. In the case of an ideal wall or without wall, a rotating tearing mode cannot produce a finite net torque on the plasma, but it can still yield a significant re-distribution of the torque in the immediate vicinity of rational surfaces, due to the continuum sound wave resonances. Here, the “re-distribution” refers to the fact that the sound wave resonance modifies (redistributes) the torque density compared to cases where the sound wave

^{a)}Electronic mail: haogz@swip.ac.cn

resonance does not occur. One such example is the zero beta plasma. In another situation, with a finite pressure plasma, the sound wave resonance may still not occur if the perturbation frequency matches the plasma flow frequency.

This finite net torque regime with a resistive wall may indeed be of practical importance for the present-day tokamaks, since almost all present-day devices as well as ITER have resistive walls surrounding the plasma, and normally the GGJ-effect is strong in these finite pressure plasmas. Therefore, the resistive wall solution is actually the most common, in practice, compared to the no-wall or ideal-wall solution, where the net torque acting on the plasma vanishes.

Following this Introduction, Sec. II briefly presents the basic formulation used in the computational model. The linear, single MHD fluid, toroidal code MARS-F¹⁵ is applied to compute the tearing mode stability and the associated EM torque. Section III reports numerical results on detailed investigation of the TM stabilization by a finite plasma pressure, on generation of the EM torque, and on parametric study of the net torque amplitude. Conclusion is drawn in Sec. IV.

II. FORMULATION

A. Resistive MHD

The linear, single fluid, toroidal MHD code MARS-F is applied to calculate the eigenvalue of the TM, as well as the associated electromagnetic torque in the presence of a resistive wall. No plasma rotation is assumed. The linearized resistive MHD equations are written as

$$\rho p^2 \xi = -\nabla P_1 + \mathbf{j} \times \mathbf{B} + \mathbf{J} \times \mathbf{Q}, \quad (1)$$

$$p\mathbf{Q} = p\nabla \times (\xi \times \mathbf{B}) - \nabla \times \eta \mathbf{j}, \quad (2)$$

$$P_1 = -\xi \cdot \nabla P - \Gamma P \nabla \cdot \xi, \quad (3)$$

$$\mathbf{j} = \nabla \times \mathbf{Q}, \quad (4)$$

where P_1 , ξ , \mathbf{j} , and \mathbf{Q} represent the perturbed pressure, plasma displacement, current, and magnetic field, respectively. ρ , \mathbf{B} , \mathbf{J} , and \mathbf{P} are the equilibrium plasma density, magnetic field, current, and pressure, respectively. η is the plasma resistivity, which is assumed a constant along the plasma minor radius. Γ is the ratio of specific heats, with $\Gamma = \infty$ corresponding to the incompressible limit.⁶ $p = \gamma + i\omega_r$ denotes the eigenvalue of the tearing mode with γ and ω_r being the mode's growth rate and real frequency, respectively. We note that ω_r can be a finite value even in a static plasma, due to the stabilization effect from the plasma pressure gradient.⁴

B. Calculation of electromagnetic torque

In this work, a straight field line coordinates (s, χ, ϕ) are adopted, where $s \equiv \sqrt{\psi_p}$ is the square root of the normalized poloidal flux ψ_p with $s = 0$ and $s = 1$ indicating the magnetic axis and the plasma boundary, respectively. χ and ϕ represent the general poloidal angle and geometrical toroidal angle, respectively. An axis-symmetric coordinate system is assumed in the present work. The perturbed magnetic field and current are written as

$$\mathbf{Q} = Q^1 \nabla \chi \times \nabla \phi + Q^2 \nabla \phi \times \nabla s + Q^3 \nabla s \times \nabla \chi, \quad (5)$$

$$\mathbf{j} = j^1 \nabla \chi \times \nabla \phi + j^2 \nabla \phi \times \nabla s + j^3 \nabla s \times \nabla \chi. \quad (6)$$

Using the above expressions, the surface averaged toroidal electromagnetic torque density, which is a function of the minor radius alone, is obtained

$$T_{j \times Q} = \frac{\pi}{J_0} \oint Re(j^1 Q^{2*} - j^2 Q^{1*}) d\chi, \quad (7)$$

where $J_0 = \oint J d\chi d\phi$ with jacobian $J = (\nabla \chi \times \nabla \phi \cdot \nabla s)^{-1}$. The symbol “*” denotes complex conjugate. We point out that the above equation is valid in an axis-symmetric coordinate equilibrium. Note that, by using the volumetric jacobian here, we define a volume averaging between two neighboring flux surfaces for the torque density.¹⁶ The above equation shows that the toroidal EM torque is determined by both the radial and poloidal components of the perturbed quantities (current and magnetic field), and is not related to the toroidal component. Equation (7) can be rewritten as a summation of all the poloidal Fourier harmonics

$$T_{j \times Q} = \frac{2\pi^2}{J_0} \sum_m [Re(j_m^1) Re(Q_m^{2*}) - Im(j_m^1) Im(Q_m^{2*}) - Re(j_m^2) Re(Q_m^{1*}) + Im(j_m^2) Im(Q_m^{1*})]. \quad (8)$$

Seven harmonics ($m = -1, 0, 1, \dots, 5$) are included for a large aspect ratio ($=10$) equilibrium considered in this work. The net toroidal EM torque, acting on the whole plasma column, is computed by (weighted) integration of the torque density along the plasma minor radius

$$TORQ1 \equiv T_{net} = \int T_{j \times Q} J_0 ds. \quad (9)$$

Alternatively, the net toroidal TM torque can also be calculated as¹²

$$TORQ2 \equiv T_{net} = \pi \oint \frac{R^2}{J} Re(Q^1 Q^{3*}) d\chi, \quad (10)$$

where the integral is carried out along any closed surface in the vacuum region between the plasma surface and the resistive wall.^{11,12} Since the EM torque generated by MHD activities is strongly localized near resonant surfaces, it is critical to ensure numerical accuracy in computing the net torque. In the results shown in this work, the net torque is always computed using both methods: the plasma volume integration method (TORQ1) and the vacuum surface integration method (TORQ2). The agreement between two methods serves as an indicator of the numerical accuracy for the torque computation.

III. NUMERICAL RESULTS

A. Equilibrium

In order to clearly demonstrate the influence of the plasma pressure on the tearing mode stability and on the

generation of the electromagnetic torque, we choose a simple toroidal equilibrium, with the aspect ratio of 10 and with a circular plasma cross section, surrounded by a resistive wall of circular shape. The plasma boundary and the wall are shown in Fig. 1. The surface averaged equilibrium current density and the equilibrium pressure are defined as functions of the poloidal magnetic flux ($s = \sqrt{\psi_p}$) as: $\langle J \rangle = J_0(1 - s^2)$ and $P = P_0(1 - s^2)^2$, respectively, where J_0 and P_0 label the current and pressure amplitudes at the magnetic axis, respectively. These values are chosen to obtain the on-axis safety factor $q_0 = 1.05$, which is fixed while scanning the normalized plasma pressure, β_N , in the computations to be shown. Here, $\beta_N \equiv \beta[\%]a[m]B_0[T]/I_p[MA]$, where $\beta = \langle P \rangle / (B_0^2/2\mu_0)$ is the ratio of the volume averaged plasma pressure to the magnetic pressure, B_0 the on-axis vacuum toroidal magnetic field, and I_p the total plasma current.

Examples of the radial profiles of the equilibrium pressure and current are shown in Fig. 2, for various choices of β_N . The corresponding q -profiles, with fixed q_0 , are plotted in Fig. 3. We notice that the plasma pressure profile significantly changes with varying β_N , whilst the current and the q -profiles almost do not change with β_N . The radial position of the $q=2$ rational surface slightly shifts inward with higher β_N . There is only one rational surface inside the plasma associated with the $n=1$ TM, for the equilibria considered here. With varying β_N , all equilibria are self-consistently obtained by running the toroidal equilibrium code CHEASE.¹⁷ The magnetic Lundquist number $S \equiv \tau_R/\tau_A = 6.3 \times 10^7$ is assumed in the computations, where $\tau_A = R_0\sqrt{\mu_0\rho_0}/B_0$, and $\tau_R = \mu_0 a^2/\eta$. Here, R_0 is the major radius of the plasma. ρ_0 is the plasma density at the magnetic axis. The plasma resistivity η is assumed to be uniform along the minor radius. The above Lundquist number corresponds to a plasma resistivity of $\eta = 1.3 \times 10^{-8}$, which is in the order of the Spitzer resistivity in typical present day tokamak plasmas.¹⁸ On the other hand, the torque physics revealed in this work does not depend on the choice of the value of the Lundquist number.

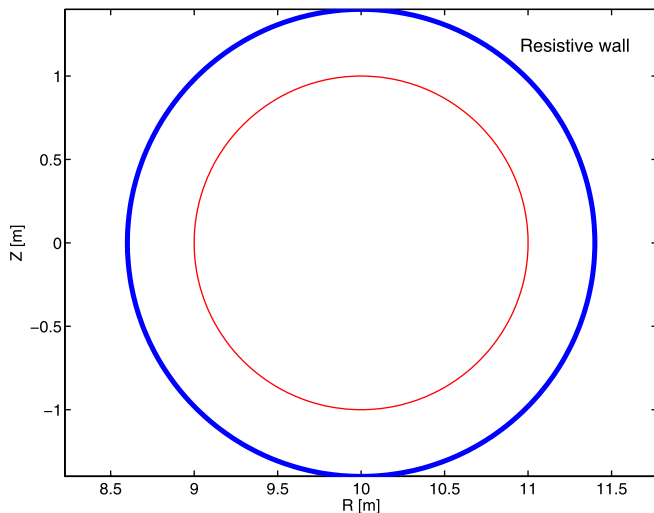


FIG. 1. The plasma boundary with a circular cross section (inner circle) and the conformal wall shape (outer circle).

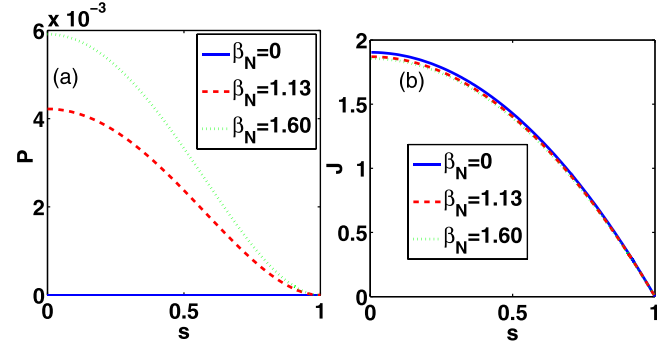


FIG. 2. Examples of radial profiles of (a) equilibrium pressure and (b) toroidal current density, with different values of the normalized plasma pressure β_N . The plasma pressure and the current are normalized by B_0^2/μ_0 and $B_0/\mu_0 R_0$, respectively.

B. Effect of finite equilibrium pressure on the tearing mode stability

The TM dispersion relation for a large aspect ratio circular plasma, including the finite plasma pressure, is given as^{4,6,19}

$$\Delta'_{int} = 2.12(1 + g)A(p\tau_A)^{5/4} \left[1 - \frac{D_R B}{1 + g} (p\tau_A)^{-3/2} \right], \quad (11)$$

where p is the TM eigenvalue, which is determined by matching Δ'_{int} (the solution in the resistive layer) and the tearing index Δ'_{ext} (the solution in the ideal region outside the resistive layer). The factors A and B are defined in Ref. 19. The factor $g = (1 - \frac{\pi}{4})|D_R|G$ is normally positive, with the G -factor being inversely proportional to the ratio of specific heats Γ . Thus, $g=0$ corresponds to the incompressible limit, whilst $g=\infty$ implies that the sound wave vanishes inside the plasma. The analytic expression for the resistive interchange index D_R was derived in Ref. 5 for a large aspect ratio equilibrium. This index is roughly proportional to the pressure gradient at the rational surface and is normally a negative number for tokamak equilibria. A negative D_R implies that the resistive interchange mode is stable and the plasma pressure in this case has a strong stabilizing effect on

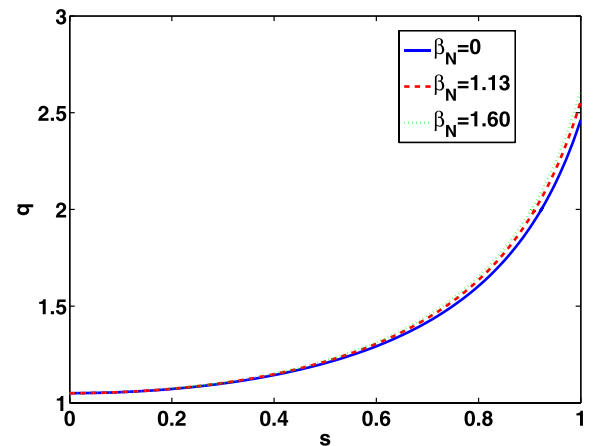


FIG. 3. Examples of radial profiles of the safety factor q with different β_N , for a large aspect ratio circular plasma. The on-axis q value is fixed at $q_0 = 1.05$.

the TM. However, for reversed field pinches, $D_R > 0$ can occur, and hence the resistive interchange mode can be destabilized by the plasma pressure.⁶

The above analytic results were obtained with specific ordering (e.g., D_R is assumed to be small). On the other hand, our numerical results shown below are obtained without assumptions of specific ordering scheme. In particular, we scan the plasma pressure up to the beta limit for the ideal kink mode. Figure 4(a) shows the MARS-F computed eigenvalues (both real and imaginary parts) of the tearing mode versus β_N , at the magnetic Lundquist number $S = 6.3 \times 10^7$ and in the presence of a resistive wall located at $b = 1.4a$. There are three distinct regions: in both the low beta (I) and high beta (III) regions, the TM is a purely growing instability, whilst in the intermediate beta values (region II), the TM is an oscillating instability (no plasma rotation is assumed in these computations). This can be explained as follows.

With real p , Δ'_{int} achieves a minimum value Δ'_{min} at certain p . As $\Delta'_{ext} > \Delta'_{min}$, the matching condition gives two real solutions, implying two purely growing resistive instabilities. As $\Delta'_{ext} < \Delta'_{min}$, the matching condition results in a pair of complex conjugate eigenvalues, implying that the tearing mode has a natural finite rotation frequency even in a static plasma.⁴ The value of Δ'_{min} is straightforwardly calculated in analytic theory (cf. Eq. (98) from Ref. 4)

$$\Delta'_{min} = 2.12(1+g)A \frac{6}{5^{5/6}} \left(\frac{-D_R B}{1+g} \right)^{5/6}, \quad (12)$$

showing that Δ'_{min} is roughly proportional to the plasma pressure (due to the fact that $|D_R|$ is roughly proportional to β_N). At $\beta_N = 0$, Δ'_{min} vanishes. On the other hand, Δ'_{ext} remains finite at $\beta_N = 0$, and approaches infinity near the no-wall beta limit for the ideal kink mode. Figure 4(b) sketches a qualitative dependence of Δ'_{ext} and Δ'_{min} on β_N , showing the possibility of the existence of three regions in the TM solution, as the plasma pressure varies.

Since Δ'_{ext} , obtained from the ideal region without the plasma rotation, is real, Δ'_{int} from the resistive layer solution, matching the outer region, must also be real. In the region near the critical point β_N^c , where $\Delta'_{ext} = \Delta'_{min}$, and the TM dispersion relation has one real solution $p = \gamma$, we perform standard perturbative analysis by setting $p = \gamma + i\omega_r$, with

$\omega_r \ll \gamma$. The requirement of Δ'_{int} being real in the region near β_N^c yields

$$\omega_r \tau_A = \pm \sqrt{\left[\frac{|D_R| B}{5(1+g)} \right]^{4/3} - (\gamma \tau_A)^2}, \quad (13)$$

where ω_r is the TM's real frequency (near β_N^c). The pair of roots shown in Eq. (13) shares the same growth rate γ , when the following condition is satisfied: $\left[\frac{|D_R| B}{5(1+g)} \right]^{4/3} > (\gamma \tau_A)^2$. Near the critical beta, the growth rate γ of the mode is also related to D_R (the gradient of the pressure at the rational surface), which is normally a negative number for tokamak equilibria. As the plasma approaches the incompressible limit $\Gamma \rightarrow \infty$ ($g \rightarrow 0$), the $\frac{1}{1+g}$ factor increases, which in turn results in the increase of the real frequency of the TM. On the other hand, as the plasma approaches the $\Gamma = 0$ limit (i.e., $g \rightarrow \infty$), $\frac{1}{1+g}$ decreases, resulting in the decrease of ω_r .

At sufficiently small Γ , $\left[\frac{|D_R| B}{5(1+g)} \right]^{4/3} < (\gamma \tau_A)^2$, and the TM becomes a purely growing mode. Hence, the presence of the sound wave (the plasma compressibility) is essential for the occurrence of a rotating TM in a static plasma (at least according to the single fluid theory) as well as for the strong stabilization of the mode by the plasma pressure.

The same results as shown in Fig. 4(a) are plotted in Fig. 5, but in the complex plane for the mode's eigenvalue. As β_N varies in the range $0.42 \leq \beta_N \leq 1.47$, two eigenvalues appear in the form of complex conjugates. We mention that similar results have been obtained in Refs. 6 and 19, while scanning the Lundquist number S instead of β_N .

When β_N is further increased beyond the no-wall limit $\beta_N^{no-wall} (= 1.69$ for our case) but still below the ideal-wall limit $\beta_N^{ideal-wall}$ for the ideal kink mode, the TM can couple with the resistive wall mode instability. Beyond the ideal-wall limit, the computed growth rate (of the ideal kink instability) is of the order $\gamma \tau_A \sim 10^{-2}$. The dependence of the resistive instability on the plasma pressure (essentially without the GGJ-effect) in the presence of a resistive wall, including the plasma rotation, is comprehensively investigated in the analytic work, Ref. 20. A further study of the

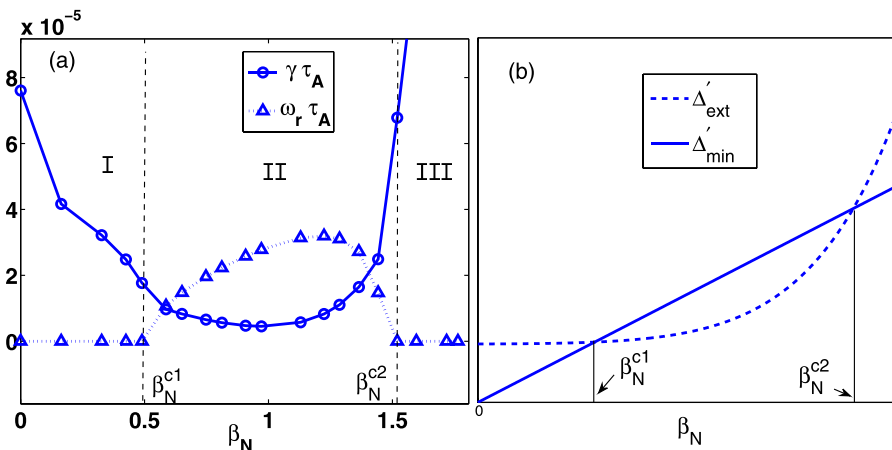


FIG. 4. (a) Normalized growth rate ($\gamma \tau_A$) and normalized real frequency ($\omega_r \tau_A$) of the tearing mode versus β_N with a resistive wall located at $b = 1.4a$. The magnetic Lundquist number S is 6.3×10^7 . No plasma rotation is assumed. And, the beta limit without a wall $\beta_N^{no-wall}$ equals to 1.69; (b) Sketching qualitative dependence of the Δ'_{ext} and Δ'_{min} on β_N .

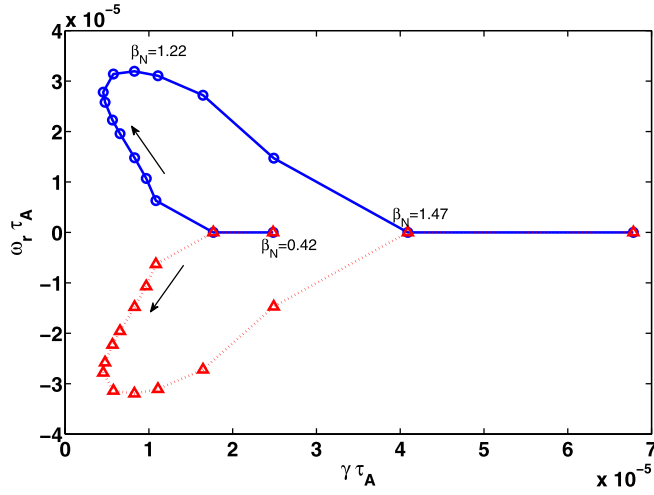


FIG. 5. The same results shown in Fig. 4 are plotted in the complex plane. The arrow in the figure labels the increasing direction of β_N .

resistive wall mode instability taking into account the GGJ-effect from the resistive layer is presented in Ref. 21.

In MARS-F computations, the wall effect on the external tearing index is automatically taken into account, when we solve the TM stability problem together with the outer-inner plasma equations as well as the wall equation, where a thin wall approximation is assumed. The above approximation implies that the skin depth of the considered mode is larger than the wall thickness. Here, we also present an analytic discussion on the dependence of Δ'_{ext} on the wall. With a resistive wall, Δ'_{ext} is expressed as²¹

$$\Delta'_{ext} = \frac{\delta_0 + \gamma \tau_w^* \delta_\infty}{\psi_0 + \gamma \tau_w^* \psi_\infty}, \quad (14)$$

where ψ_0 and ψ_∞ denote the perturbed magnetic flux at the rational surface without a wall and with an ideal wall, respectively. While δ_0 and δ_∞ are the jumps of ψ_0 and ψ_∞ at the rational surface, respectively. The definition of the wall time is $\tau_w^* = bd\sigma\mu_0$, with b , d , σ , and μ_0 being the plasma

minor radius, the wall thickness, the wall conductivity, and the permeability of free space, respectively. The derivative of Δ'_{ext} to the wall time τ_w^* is

$$\frac{d\Delta'_{ext}}{d\tau_w^*} = \gamma \frac{\delta_\infty \psi_0 - \psi_\infty \delta_0}{(\psi_0 + \gamma \tau_w^* \psi_\infty)^2}. \quad (15)$$

Hence, the sign of the above derivative is determined by the mode's growth/damping rate and the sign of $\delta_\infty \psi_0 - \psi_\infty \delta_0$. In this work, the tearing mode is unstable in the whole β_N region without a wall, which implies $\psi_0 > 0$ and $\delta_0 > 0$. In addition, the kink mode is stable, which implies $\psi_\infty > 0$. Furthermore, due to the slight stabilization of the ideal wall on the unstable tearing mode, we expect the condition $\frac{\delta_0}{\psi_0} > \frac{\delta_\infty}{\psi_\infty} \Rightarrow \delta_\infty \psi_0 - \delta_0 \psi_\infty < 0$. Hence, for the case with unstable tearing mode (i.e., $\gamma > 0$) the parameter Δ'_{ext} decreases with increasing the wall time τ_w^* , as expected.

The eigenfunctions of the TM are quite different in the three regions I, II, and III of β_N shown in Fig. 4. Figures 6–8 plot three representative eigenfunctions for three chosen β_N values: $\beta_N = 0$, $\beta_N = 1.13$, and $\beta_N = 1.6$, from the regions I, II, and III, respectively. The radial profiles of the poloidal Fourier harmonics of the plasma radial displacement are compared. We make the following observations: (1) For the pressure-less case $\beta_N = 0$, the (unstable) TM is driven by the gradient of the equilibrium current density. The eigenfunction of this conventional type of TM is plotted in Fig. 6, showing a dominate poloidal harmonic ($m = 2$) for the radial displacement, localized near the $q = 2$ rational surface. (2) For the oscillating TM in the intermediate pressure range, the $m = 3$ sideband is enhanced. The coupling of the TM to the kink components begins to appear. (3) With further increase of the plasma pressure ($\beta_N = 1.60$), the kink components come significant in the plasma displacement, although at the rational surface, the resistive component is still dominant. The $m = 3$ sideband is further (slightly) enhanced at the rational surface.

Because of the sensitive dependence of the TM behavior on the plasma compressibility as discussed above (as well as in Ref. 4), we also compute the TM eigenvalue, while

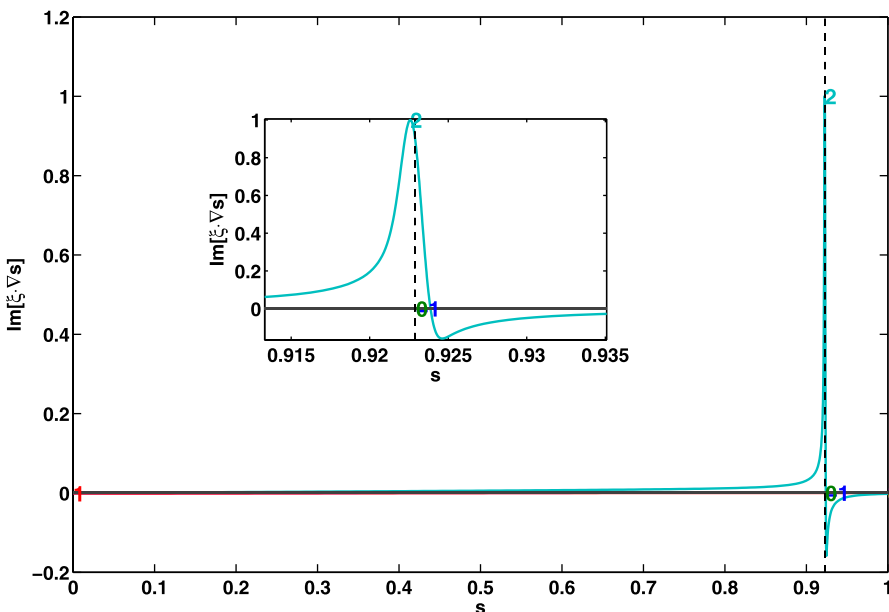


FIG. 6. The eigenfunction of the TM for $\beta_N = 0$ with a resistive wall located at $b = 1.4a$, in the absence of the plasma flow. The magnetic Lundquist number S is 6.3×10^7 . Here, the MARS-F computed TM's growth rate $\gamma \tau_A$ is 7.61×10^5 . The vertical dashed line denotes the location of the $q = 2$ rational surface. Here, the normalized wall time τ_w ($\tau_w = \tau_w^*/\tau_A$) equals to 2×10^4 .

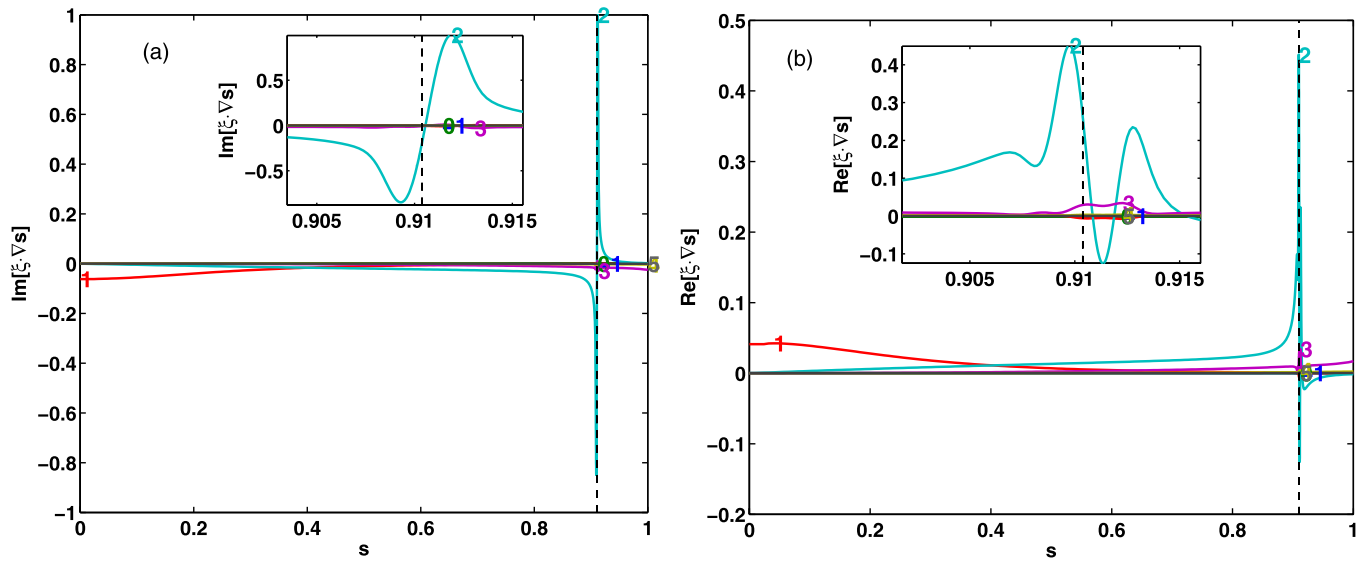


FIG. 7. (a) The imaginary part and (b) real part of the eigenfunction of the modified TM for $\beta_N = 1.13$ for the static toroidal plasma surrounded by a resistive wall located at $b = 1.4a$. The MARS-F computed normalized TM's eigenvalue is $5.76 \times 10^{-6} + i3.14 \times 10^{-5}$. The magnetic Lundquist number S is 6.3×10^7 . The vertical dashed line denotes the location of the $q = 2$ rational surface.

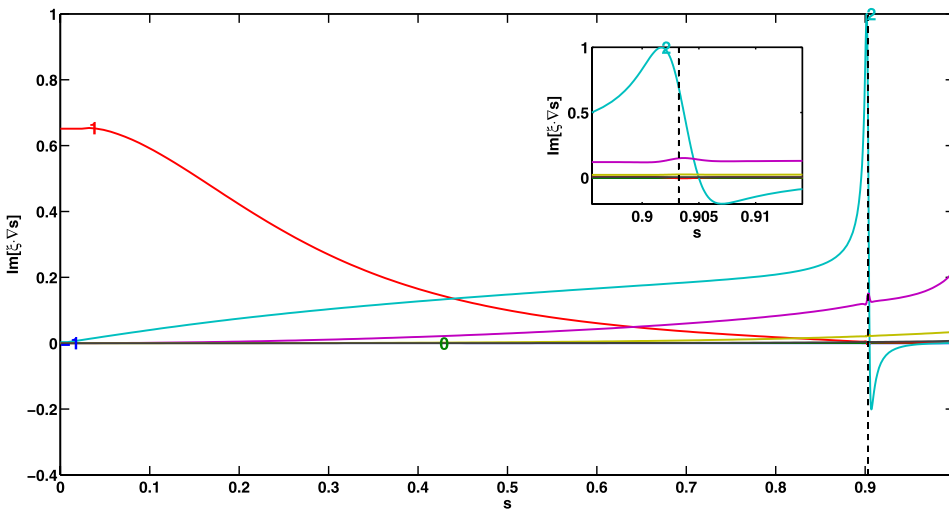


FIG. 8. The eigenfunction of the TM for $\beta_N = 1.60$. The TM's normalized growth rate is 1.16×10^{-4} . The vertical dashed line denotes the location of the $q = 2$ rational surface.

varying the ratio of specific heats Γ . The results are shown in Fig. 9. When Γ is smaller than a critical value Γ_c , the computed TM is purely growing, with two real eigenvalues as predicted by theory. Above the critical value, the computed eigenvalues again become complex numbers, with the real frequency of the mode increasing with Γ . At sufficiently large Γ , the eigenvalue saturates to the incompressibility limit. It is interesting to notice that the finite mode frequency remains at this limit.

The above numerical observation can be qualitatively understood as follows. Since Δ'_{ext} is almost independent of Γ , it can be considered as a constant with varying Γ . On the other hand, Δ'_{int} sensitively depends on Γ via the G factor as shown in Eq. (12). Consequently, the region $\Gamma < \Gamma_c$ ($\Gamma > \Gamma_c$) corresponds to $\Delta'_{ext} > \Delta'_{min}$ ($\Delta'_{ext} < \Delta'_{min}$).

C. Electromagnetic torque generated by tearing mode

A rotating TM in a static plasma can generate electromagnetic torque acting on the plasma. In the presence of an

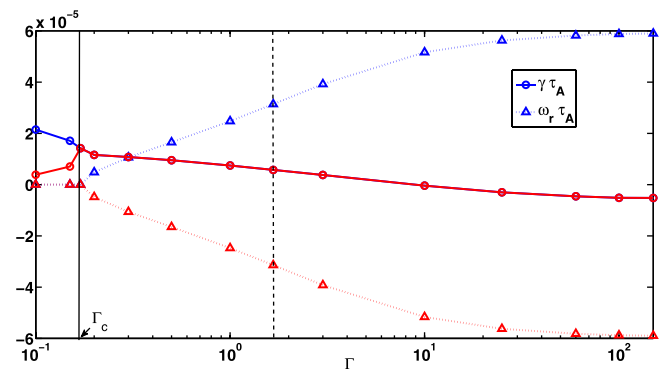


FIG. 9. The eigenvalues of the TM versus the ratio of specific heats Γ . $\Gamma = \infty$ corresponds to the incompressibility limit. The vertical dashed line labels the position of $\Gamma = 5/3$. The vertical solid line denotes the position of the critical point Γ_c . The solid curves denote the mode's growth rate, and the dashed curves label the mode's real frequency.

ideal wall, or in the absence of any wall, the net torque acting on the plasma column should vanish due to the momentum conservation constraint. However, in the presence of a resistive wall surrounding the plasma, a net torque can be generated on the plasma, which is compensated by the finite torque acting on the wall due to the presence of the eddy current flowing in the wall. This is numerically verified here. Figure 10 shows the MARS-F computed net toroidal electromagnetic torque (over the whole plasma column) as a function of β_N , using the eigenfunctions computed in Fig. 4. The torque is evaluated using the solution of an eigenvalue problem. Here, in order to ensure a relative comparison of the torque strength as we scan certain parameters (e.g., β_N in Fig. 10 or τ_w in Fig. 14), we need to define a proper normalization for the net torque amplitude. A natural choice is the perturbed kinetic energy (i.e., the plasma inertia $E = \int \rho_0 |\xi|^2 J ds d\chi d\phi$), which scales as the square of the amplitude of the linear perturbation, the same as the torque itself. Hence, the proper normalization of the net torque (i.e., T_{net}/E) does not depend on the arbitrary amplitude of the linear perturbation, which is related to the phase difference between Q^1 and Q^3 and to the equilibrium parameters. We point out that the net torques shown in the figures below are the normalized values. It is evident that only in region II, where the eigenvalue of the TM is a complex number, there is a finite net EM torque acting on the static plasma in the toroidal direction. Also note very good agreement between the two different methods computing the net torque, namely the volumetric integration method (TORQ1) and the surface integration method (TORQ2) as described in early discussion. This verifies the numerical accuracy of the net torque computations, which is computationally challenging due to the presence of a very narrow resistive layer. We also verified that the value of TORQ2 does not depend on the choice of the integration surface in the vacuum region (between the plasma and the resistive wall), as expected.

The net torque reaches its peak value at $\beta_N = 1.13$. The direction of the net torque is always opposite to that of TM rotation. We emphasize that the eventual physics associated

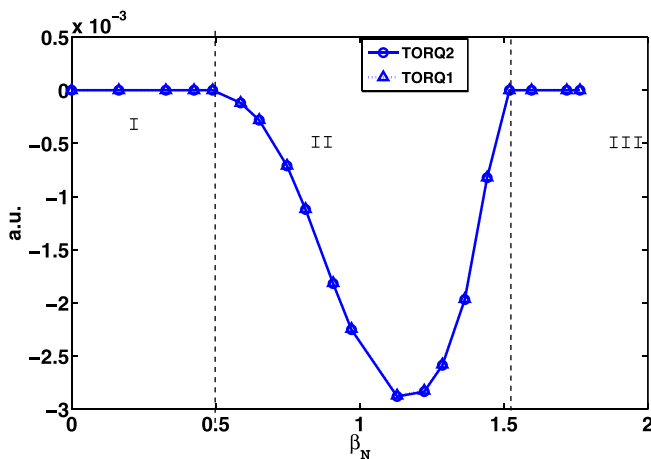


FIG. 10. The normalized net toroidal electromagnetic torque versus β_N . TORQ1 (dashed symbol curve) and TORQ2 (solid symbol curve) denote the results obtained by the volume integration method (Eq. (9)) and surface integration method (Eq. (10)), using the eigenfunctions computed in Fig. 4.

with the electromagnetic torque, which we study in this work, is different from that presented in Refs. 7–10, where a so called constant-psi approximation is assumed, which is strictly valid only for equilibria with vanishing pressure gradient near the mode's rational surface. This theory always predicts zero net torque due to the TM in a static plasma. The theory from Ref. 11, on the other hand, simply assumes that the mode's frequency is known, without elaboration on the physics that leads to the assumed mode's frequency. However, the rotation of the tearing mode in this work is induced by the GGJ-effect, and the associated finite net torque can potentially *drive* flow in the plasma, which we assume to be initially in a static equilibrium state.

The conservation of the total momentum requires that an equal amount of toroidal torque to be generated inside the resistive wall.¹¹ To verify this, we choose a vacuum surface *enclosing* both the plasma and the resistive wall for performing the surface integration, Eq. (10), for the case of $\beta_N = 1.13$. The computed toroidal torque indeed vanishes. Furthermore, from Fig. 9, one can deduce that a finite net EM torque inside the plasma remains in the incompressible limit, but vanishes in the limit of $\Gamma = 0$.

Next, we investigate the radial distribution of the toroidal EM torque, generated by the rotating TM mode in a static plasma. Since the torque is mainly localized within the resistive layer, we shall show the torque density profile in the vicinity of rational surface. Figure 11(a) compares the torque density for two cases, with $\beta_N = 0.54$ and $\beta_N = 1.13$. We observe that the torque density has detailed radial structures, with several local peaks and sharp variations within the resistive layer. This also implies a significant cancellation along the radial integration of the torque density, although a finite (volumetric) net torque remains in the presence of a resistive wall.

Detailed radial structures of the EM torque can also be generated by an externally applied static resonant magnetic perturbation (RMP) field on a *rotating* plasma. For instance, Ref. 12 finds odd and even parity profiles associated with the sound wave and shear Alfvén wave resonances, respectively. In the present study, the plasma is *static* but the TM is rotating, which also creates the possibility of continuum resonances. However, since the mode rotating frequency is rather small ($\omega_r \tau_A = 3.14 \times 10^{-5}$ for the case of $\beta_N = 1.13$)

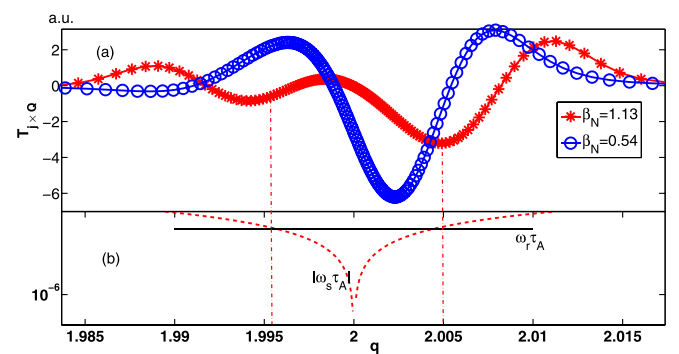


FIG. 11. (a) The electromagnetic torque density versus the safety factor q for two chosen cases $\beta_N = 1.13$ and $\beta_N = 0.54$. The MARS-F computed TM's eigenvalue are $5.76 \times 10^{-6} + i3.14 \times 10^{-5}$ and $1.08 \times 10^{-5} + i6.31 \times 10^{-6}$, respectively. (b) The sound wave frequency $|\omega_s \tau_A|$ versus the safety factor q and the mode frequency $\omega_r \tau_A = 3.14 \times 10^{-5}$ for $\beta_N = 1.13$.

compared to the usual plasma rotation frequency, the Alfvén resonant splitting effect, observed in Ref. 12 for a rotating plasma, is almost negligible here. The sound wave resonant splitting is still possible as shown by Fig. 11(b). In either case, the resonance is “smoothed” by the presence of the finite mode growth rate of the TM. This probably explains the less clear parity trend shown in Fig. 11(a).

The sound resonance splitting, shown in Fig. 11(b), occurs at the radial positions where the real frequency $\omega_r \tau_A$ of the mode equals to the sound frequency $\omega_s \tau_A$, defined here as (using a straight cylinder model)

$$\omega_s^2 = \frac{(m/q - n)^2 V_s^2}{\tau_A^2 \hat{\rho} (V_s^2 F_{PS} + V_A^2)}, \quad (16)$$

where $V_A \equiv B_0 / \sqrt{\mu_0 \rho}$ is the Alfvén velocity, and $V_s \equiv \sqrt{\Gamma P / \rho}$ is the sound velocity. $\hat{\rho} \equiv \rho / \rho_0$ is the normalized plasma density. $F_{PS} = 1 + q^2 / (m - 1 - nq)^2 + q^2 / (m + 1 - nq)^2$ is Pfirsch-Schluter factor representing the inertial enhance effect, where m is the resonant poloidal harmonic. 22 The resonant condition $|\omega_r| = |\omega_s|$ roughly predicts two resonant locations at $q = 1.996$ and 2.005 , respectively, for the case of $\beta_N = 1.13$ as shown in Fig. 11(b).

For the other case of $\beta_N = 0.54$, the real frequency of the TM is even smaller ($\omega_r \tau_A = 6.31 \times 10^{-6}$), and the sound wave resonant locations ($q = 1.999$ and 2.001) are even closer to the rational surface. The two odd parity shapes roughly merge to form an even parity profile. Figure 11 shows that the torque density profile strongly depends on the frequency of the TM, which determines the resonant locations.

The torque density with sharply varying radial profiles can, in principle, result in strong flow shear in the immediate vicinity of the resistive layer. The torque localized near the rational surface can eventually be transported to the other plasma region through the momentum transport mechanisms, 23 or through the viscous torque balance. 9,24

The detailed radial structures of the torque density near the rational surface are related to the local profiles of the perturbed current density and the magnetic field. Figure 12 shows the radial profiles of the perturbed current components, including both the real and imaginary parts (in the complex representation of the perturbed quantities), for the $\beta_N = 1.13$ case. All the components are subject to a global normalization, allowing a relative comparison of the amplitude of various components. The amplitude of the radial component (j^1) of the perturbed current is much smaller than that of the other components as expected, and is determined by the perturbed current conservation. The amplitude of the poloidal component (j^2) is about six times larger than the toroidal component (j^3). For either j^1 or j^2 , the dominant contribution comes from the resonance harmonic $m = 2$. However, for the toroidal component, the main contribution is the side-band harmonics $m = 1$ and 3 , which are almost the same in both the amplitude and the sign. This indicates that the sound wave resonance mainly enhances the toroidal coupling of the side-band harmonics for the toroidal component of the perturbed current.

Figure 13 shows the radial profiles of the perturbed magnetic fields, for the same case as Fig. 12. The amplitude of toroidal component is much smaller than the other two components, as it should be for this type of large aspect ratio

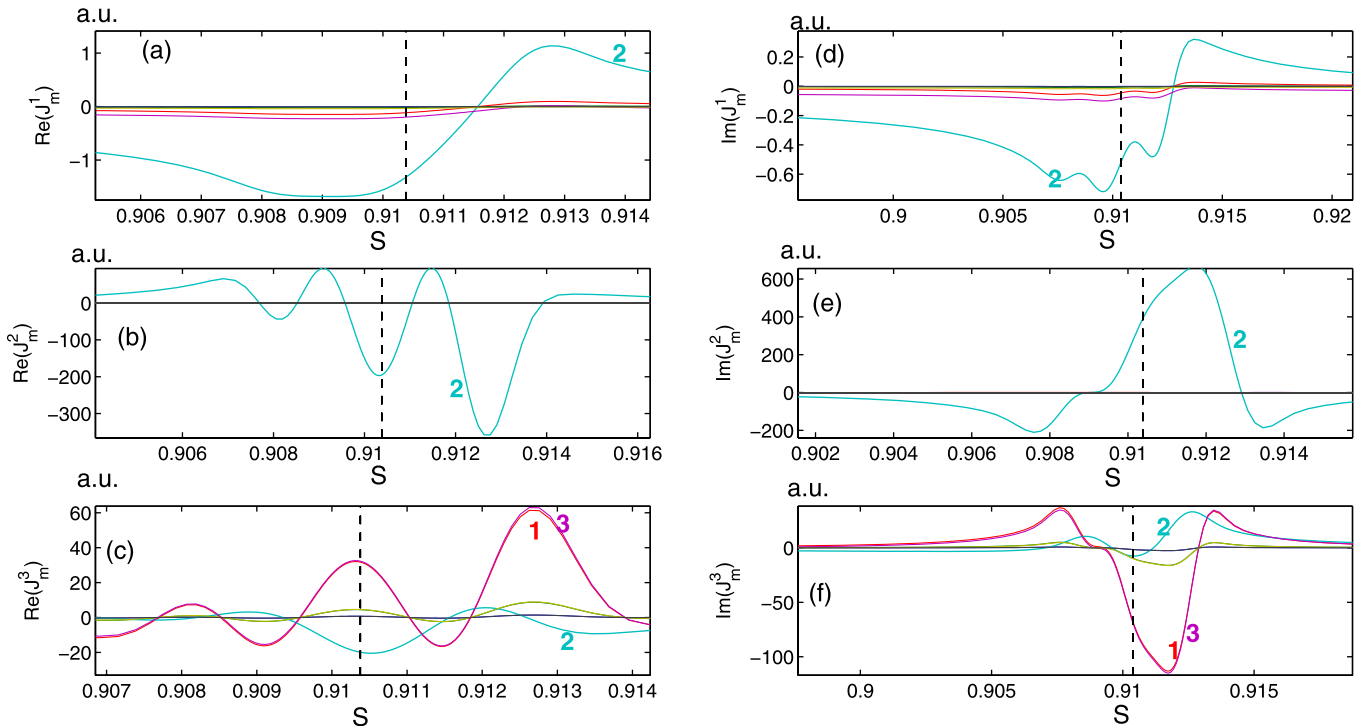


FIG. 12. The radial profiles of the poloidal Fourier harmonics of the perturbed current in the resistive layer, for the real part of (a) radial, (b) poloidal, and (c) toroidal components, respectively, and for the imaginary part of (d) radial, (e) poloidal, and (f) toroidal components, respectively. Here, $\beta_N = 1.13$. The vertical line labels the location of the $q = 2$ rational surface. It is noted that the relative amplitudes between different field components, shown in this figure, are fixed by the eigenmode structure.

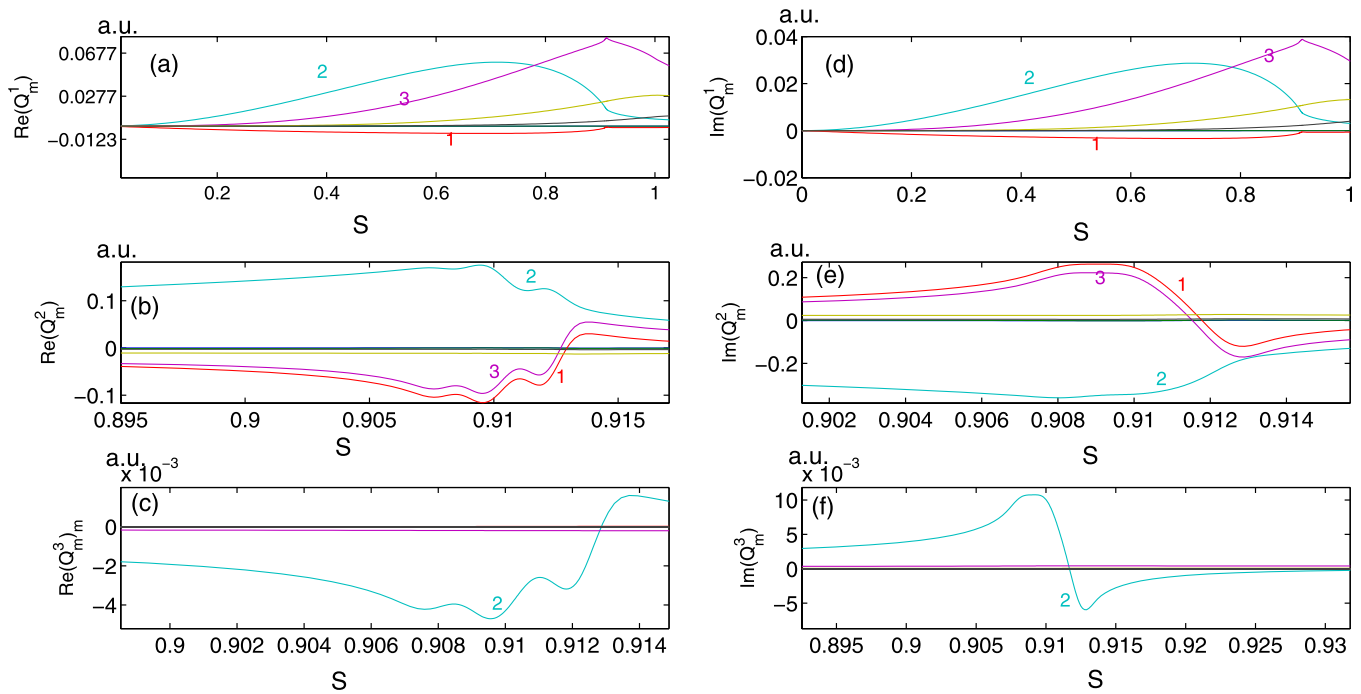


FIG. 13. The radial profiles of the poloidal Fourier harmonics of the perturbed magnetic field, for the real part of (a) radial, (b) poloidal, and (c) toroidal components, respectively, and for the imaginary part of (d) radial, (e) poloidal, and (f) toroidal components, respectively. Here, $\beta_N = 1.13$. It is noted that the relative amplitudes between different field components, shown in this figure, are fixed by the eigenmode structure.

equilibrium (the toroidal perturbation vanishes in a straight cylinder). We notice that the radial field perturbation is global, whilst the poloidal and toroidal components are largely localized in the resistive layer, without violating the divergence-free condition. This is mainly because the radial field component has a strong radial variation inside the resistive layer, which “gives rise to” a large amplitude of the tangential components inside the layer. This is different from a conventional case of the constant- ψ approximation for the radial field inside the resistive layer—the radial field is far from constant inside the layer when this is a finite equilibrium pressure gradient across the rational surface.

For the poloidal component, the amplitude of the side-band harmonics $m = 1, 3$ is in the same order as that of the resonant harmonic $m = 2$. Combining the radial profiles shown in Figs. 12 and 13 and expression (8), we find that the electromagnetic torque density, as shown in Fig. 11(a) for

the $\beta_N = 1.13$ case, mainly comes from the resonant harmonics $m = 2$ of j^2 and Q^2 . Indeed, the torque profile in the vicinity of the resonant surface resembles that of the $m = 2$ harmonic of the perturbed poloidal current density j^2 .

D. Effect of wall on the TM generated net torque

The momentum balance between the plasma and the resistive wall is crucial for determining the amplitude of the normalized net EM torque acting on the plasma. In this subsection, we investigate the dependence of the normalized net torque on the wall parameters, including the wall position and the wall time. Figure 14 plots the TM’s eigenvalue and the net torque as functions of the normalized wall time ($\tau_w \equiv \tau_w^*/\tau_A$). In Fig. 14, the wall time varying by 7 orders of magnitude physically corresponds to the variation of the wall conductivity, while the wall thickness is fixed at about

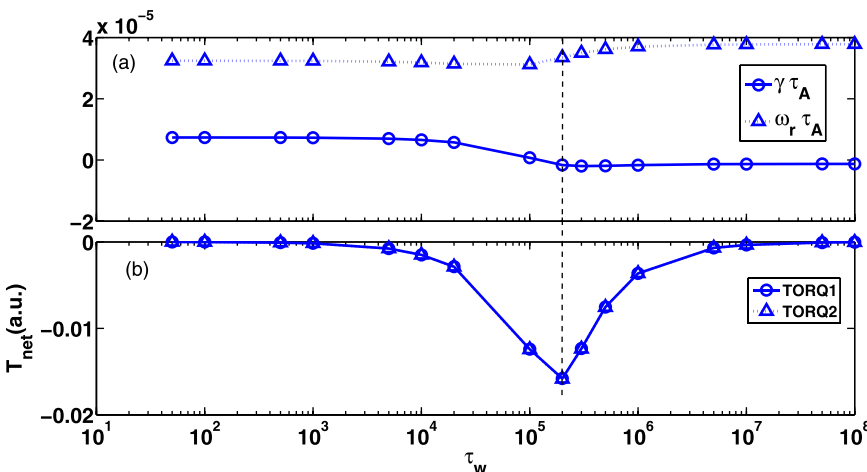


FIG. 14. (a) The eigenvalue of the tearing mode and (b) normalized net toroidal electromagnetic torque versus the wall time τ_w for $S = 6.3 \times 10^7$, $\beta_N = 1.13$, and $b = 1.4a$.

0.001 of the plasma minor radius. This ensures that the thin wall approximation is valid for all the chosen wall times in this study. The limit of $\tau_w \rightarrow 0$ corresponds to the no wall case, whilst $\tau_w \rightarrow \infty$ corresponds to the ideal wall limit. At small wall time $\tau_w < 10^4$, no considerable net electromagnetic torque is generated by the resistive instability. In this case, the induced eddy current in the resistive wall is negligible, yielding also negligible EM torque on the wall and hence the net torque on the plasma. A wall with low conductivity hardly contributes considerable stabilization effect on the TM. In the other limit, when the conductivity of the wall is too large (close to an ideal wall), the induced eddy current in the wall tends to generate a perturbed radial magnetic field, which exactly cancels the perturbed radial magnetic field generated by the rotating tearing mode, resulting in a vanishing radial magnetic in the wall (also see Fig. 16). Hence, at the ideal wall limit, the electromagnetic torque in the wall also vanishes. The momentum conservation constraints imply a zero net torque on the plasma in this case.

As the wall time (from $\sim 2 \times 10^4$ to $\sim 2 \times 10^6$) is in the same order as the time scale of the TM's oscillation ($(\tau_{mode} \equiv \frac{2\pi}{\omega_r \tau_A} \simeq 2 \times 10^5)$), the wall significantly stabilizes the tearing mode. When $\tau_w \simeq \tau_{mode}$, the net torque generated by the TM reaches its maximum, implying also the maximal momentum exchange between the plasma and the wall. In fact, in a circular cylinder, Eq. (42) from Ref. 14 indicates that the EM force on the plasma is proportional to $|\omega_r| \tau_w^* / [1 + (|\omega_r| \tau_w^*)^2]$, showing that indeed the maximal torque is achieved when the wall time normalized perturbation frequency reaches an order one value. Furthermore, Fig. 14 shows that when $\tau_w \geq 2 \times 10^5$, the TM is fully stabilized, and the real frequency of the mode slightly increases. At $\tau_w = \infty$, the TM reaches its ideal wall stability limit, which is stable in our case.

In the no-wall and the ideal wall limit, there is no momentum exchange between the wall and the plasma, and there is no net electromagnetic torque on the plasma. On the other hand, due to the presence of a rotating TM, the sound wave resonance still results in a re-distribution of the EM torque within the plasma as shown in Fig. 15. This local re-distribution may still generate rotation shear in the vicinity of the rational surface, without external momentum input.

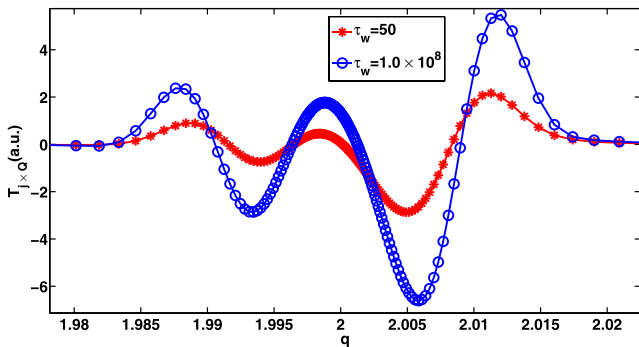


FIG. 15. The radial profiles of the electromagnetic torque for the wall time $\tau_w = 50$ and $\tau_w = 1.0 \times 10^8$ with the corresponding eigenvalues $7.37 \times 10^{-6} + i3.24 \times 10^{-5}$ and $-1.27 \times 10^{-6} + i3.78 \times 10^{-5}$, respectively. Here, $S = 6.3 \times 10^7$, $\beta_N = 1.13$, and $b = 1.4a$.

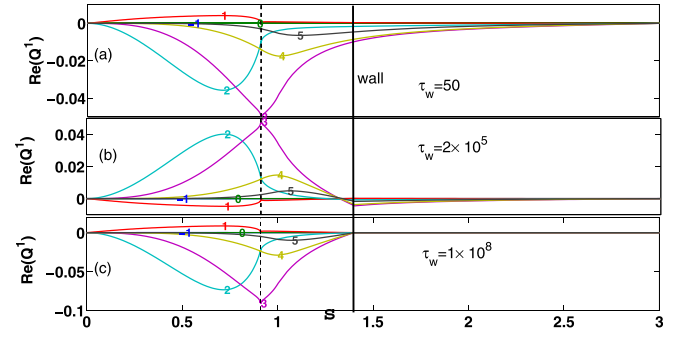


FIG. 16. Radial profiles of the poloidal Fourier harmonics of the radial component of the perturbed magnetic field for (a) $\tau_w = 50$, (b) $\tau_w = 2 \times 10^5$, and (c) $\tau_w = 10^8$. Here, in the plasma, the s labels the normalized poloidal flux, and in the region outside the plasma, the s labels the minor radial position normalized to the plasma minor radius. The vertical dashed line denotes the $q = 2$ resonant surface. The vertical solid line labels the location of the resistive wall.

Figure 16 shows the radial profiles of the perturbed radial magnetic field Q^1 for three cases of $\tau_w = 50$, 2×10^5 , and 10^8 , respectively. At $\tau_w = 50$ (small wall time), the perturbed magnetic field easily penetrates through the wall. At $\tau_w = 2 \times 10^5$, the presence of the resistive wall significantly reduces the penetration of the field. At $\tau_w = 10^8$ (large wall time), the wall appears as nearly an ideal wall, and the radial field does not penetrate through.

The dependence of the TM eigenvalue and the net electromagnetic torque on the wall position is plotted in Fig. 17. Both growth rate and real frequency of the mode monotonically increase with the wall position b . The amplitude of the net torque monotonically decreases with b . As the wall moves closer to the plasma surface, the TM can be stabilized, and the resulting net torque substantially increases. As the resistive wall moves farther away from the plasma, we recover the no-wall results, with a vanishing net torque on the plasma. We point out that the presence of a resistive wall (i.e., neither an ideal wall nor the absence of a wall) is most common in present tokamak devices. Therefore, the resistive wall case, where the TM can generate a finite net torque, represents the most applicable situation in practice.

IV. CONCLUSION AND DISCUSSION

In this work, we have numerically investigated the effect of the plasma pressure on the tearing mode stability and on the generation of the toroidal electromagnetic torque acting on a static toroidal plasma. It is demonstrated that three different linear TM stability regimes can be achieved, before reaching the beta limit for ideal instability. In an intermediate pressure regime, the linear tearing mode, in a static plasma, has a real frequency due to the GGJ-effect. The presence of the sound wave is necessary for stabilizing the tearing mode through the plasma pressure term. With further increase of the plasma pressure, it has a strong destabilization effect on the mode, which is largely due to the modification of the (linear) tearing index associated with the outer solution. Generally, increasing the plasma pressure helps to couple the TM to global kink structures.

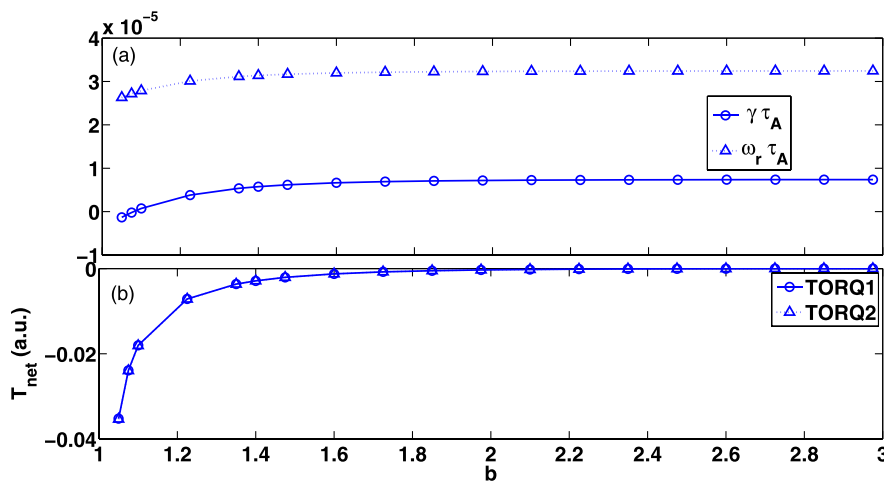


FIG. 17. (a) The MARS-F computed eigenvalue of the tearing mode and (b) normalized net toroidal electromagnetic torque versus wall minor radius b , for $S = 6.3 \times 10^7$, $\beta_N = 1.13$, and $\tau_w = 2.0 \times 10^4$.

A rotating tearing mode further results in a re-distribution of the toroidal electromagnetic torque, with multiple local peaks in the immediate vicinity of the resistive layer. The sound wave resonances play a role in this torque re-distribution. In the presence of a resistive wall surrounding the plasma, a rotating TM generates a finite net electromagnetic torque on the plasma column, which compensates the eddy current induced torque in the resistive wall. When the wall time matches the oscillating time scale of the tearing mode, the net torque reaches maximum. At the no-wall or ideal wall limit, no net torque is generated, yet a significant re-distribution of the toroidal torque still occurs in the resistive layer.

Since the linear TMs in present day tokamaks are often in the GGJ-regime, and almost all the devices have a resistive wall surrounding the plasma, the presence of the TM generated finite net EM torque should represent a generic situation. The remaining questions are how fast such a net torque can drive the plasma flow, and how the generated plasma flow can act back to affect the TM stability. These aspects will be investigated in the near future, using the quasi-linear code MARS-Q.²⁵

ACKNOWLEDGMENTS

This work was supported by National Natural Science Foundation of China (No. 11205051, No. 11175057, No. 11275061, and No. 11205053) and by National Magnetic Confinement Fusion Science Program (No. 2014GB124004 and No. 2011GB105002). This work was part-funded by the RCUK Energy Programme under grant EP/I501045 and the European Communities under the contract of Association between EURATOM and CCFE. The views and opinions expressed herein do not necessarily reflect those of the European Commission. G.Z.H. acknowledges the hospitality

of Euratom/CCFE Fusion Association, where part of this work was completed.

- ¹Y. Nishimura, J. D. Callen, and C. C. Hegna, *Phys. Plasmas* **5**, 4292 (1998).
- ²Y. Nishimura and M. Azumi, *Phys. Plasmas* **4**, 2365 (1997).
- ³M. S. Chu, R. J. La Haye, M. E. Austin, L. L. Lao, E. A. Lazarus, A. Pletzer, C. Ren, E. J. Strait, T. S. Taylor, and F. L. Waelbroeck, *Phys. Plasmas* **9**, 4584 (2002).
- ⁴A. H. Glasser, J. M. Greene, and J. L. Johnson, *Phys. Fluids* **18**, 875 (1975).
- ⁵A. H. Glasser, J. M. Greene, and J. L. Johnson, *Phys. Fluids* **19**, 567 (1976).
- ⁶T. C. Hender, R. J. Hastie, and D. C. Robinson, *Nucl. Fusion* **27**, 1389 (1987).
- ⁷R. Fitzpatrick and T. C. Hender, *Phys. Fluids B* **3**, 644 (1991).
- ⁸R. Fitzpatrick, *Phys. Plasmas* **5**, 3325 (1998).
- ⁹B. E. Chapman, R. Fitzpatrick, D. Craig, P. Martin, and G. Spizzo, *Phys. Plasmas* **11**, 2156 (2004).
- ¹⁰R. Fitzpatrick, S. C. Guo, D. J. D. Hartog, and C. C. Hegna, *Phys. Plasmas* **6**, 3878 (1999).
- ¹¹V. D. Pustovitov, *Nucl. Fusion* **47**, 1583 (2007).
- ¹²Y. Q. Liu, J. W. Connor, S. C. Cowley, C. J. Ham, R. J. Hastie, and T. C. Hender, *Phys. Plasmas* **19**, 102507 (2012).
- ¹³N. C. Logan, E. J. Strait, and H. Reimerdes, *Plasma Phys. Controlled Fusion* **52**, 045013 (2010).
- ¹⁴R. Fitzpatrick, *Nucl. Fusion* **33**, 1049 (1993).
- ¹⁵Y. Q. Liu, A. Bondeson, C. M. Fransson, B. Lennartson, and C. Bretholtz, *Phys. Plasmas* **7**, 3681 (2000).
- ¹⁶W. Dhaeseleer, W. Hitchon, J. Callen, and J. Shohet, *Flux Coordinates and Magnetic Field Structure. A Guide to a Fundamental Tool of Plasma Theory* (Springer-Verlag, Berlin, 1991).
- ¹⁷H. Lutjens, A. Bondeson, and O. Sauter, *Comput. Phys. Commun.* **97**, 219 (1996).
- ¹⁸J. Wesson, *Tokamaks*, 3rd ed. (Oxford University Press, 2004).
- ¹⁹Y. Liu, J. Connor, S. C. Cowley, C. J. Ham, R. J. Hastie, and T. C. Hender, *Phys. Plasmas* **19**, 072509 (2012).
- ²⁰R. Betti, *Phys. Plasmas* **5**, 3615 (1998).
- ²¹A. Bondeson and H. X. Xie, *Phys. Plasmas* **4**, 2081 (1997).
- ²²C. Wahlberg and A. Bondeson, *J. Plasma Phys.* **57**, 327 (1997).
- ²³C. Angioni, *Plasma Fusion Res.* **8**, 2102032 (2013).
- ²⁴R. Fitzpatrick, R. Takahashi, R. J. Hastie, T. J. Martin, and C. M. Roach, *Nucl. Fusion* **33**, 1533 (1993).
- ²⁵Y. Liu and Y. Sun, *Phys. Plasmas* **20**, 022505 (2013).